

Anelastic dynamo models with variable electrical conductivity: an application to gas giants

Lúcia D. V. Duarte^{1,2}, Thomas Gastine¹, Johannes Wicht¹

Max-Planck-Str. 2, 37191 Katlenburg-Lindau, Germany

Abstract

Observations of the two gas giants show that both planets have dipolar magnetic fields: Jupiter's is very similar to Earth's magnetic field and Saturn's is very axisymmetric. Our main goal is to construct realistic numerical models that explain these features.

While the small density jump across terrestrial iron cores allows to use the Boussinesq approximation, the picture is different for the gas giants. Here, the density decreases by a factor of around 5000 from the deep interior to the surface (1 bar level). Though most of this density jump is accommodated in the outer molecular envelopes, it may still be significant in the metallic dynamo region. Among other properties, the electrical conductivity also varies significantly with radius, being roughly constant in the metallic hydrogen region and decaying exponentially in the molecular envelope. We solve an anelastic numerical dynamo model (which differs from a fully compressible model by neglecting sound waves) to explore the effects of density stratification and electrical conductivity variation on magnetic field generation.

We use an anelastic version of the MHD code MagIC with density jumps up to 245 and an electrical conductivity that decays exponentially in the outer 5–30% of the simulated shell. Previous simulations using constant conductivity showed that dipole-dominated magnetic fields are only found up to a density jump of 6. An increasing stratification progressively confines the most active convective region close to the outer boundary equator. Mean field models have shown that such a configuration prefers non-axisymmetric modes. The exponential conductivity decrease helps by separating magnetic field generation from the dominant convective region.

For intermediate stratifications ($6 < \text{density jump} < 148$), the dipole component clearly dominates during short periods. Stable strongly dipolar solutions are found either when a large stratification (density jump > 148), at $E = 10^{-4}$, more clearly separates the dynamo from the dominant convective region, or when lower Ekman number are considered.

Keywords:

Atmospheres, dynamics, Jupiter, interior, Variable electrical conductivity, Numerical dynamos

1. Introduction

The dipolar magnetic fields of the gas giants, Jupiter and Saturn, are generated in their deeper interiors. Both planets mainly consist of a hydrogen-helium mixture. Due to the large pressures and temperatures reached inside these planets, hydrogen acquires metallic properties and becomes electrically conducting (Chabrier et al., 1992; Fortney and Nettelmann, 2010). The transition happens at 85–90% of Jupiter's and 65% of Saturn's radii. The traditional view is that the lower metallic envelope likely hosts the dynamo of these planets, while the upper molecular envelope accommodates the observed fierce zonal jets. Higher densities, Lorentz forces and Ohmic diffusion would lead to a more sluggish dynamics in the metallic envelope and confine the zonal winds to the upper region. Traditional dynamical models therefore treat the two envelopes separately with dynamo simulations modeling only the metallic envelope and jet simulations concentrating on the molecular region.

The zonal jets have been investigated since the 70s by tracking cloud features (see, for example, Ingersoll et al., 1979 for Jupiter and Sanchez Lavega, 1982 for Saturn). Their driving forces and depth are still debated. Some authors argue that they are a shallow weather phenomenon (Williams, 1978; Cho and Polvani, 1996) while others promote deeper-rooted jets that extend through the whole molecular envelope (Heimpel et al., 2005; Jones and Kuzanyan, 2009; Gastine and Wicht, 2012). Gas giants emit roughly twice as much energy as they receive from the sun which argues for vigorous interior convection. In the rotationally-dominated dynamics ruling planetary atmospheres, interior convection quite naturally drives zonal winds via Reynolds stresses (i.e. a statistical correlation between the convective flow components; Christensen, 2002; Heimpel et al., 2005). The winds follow a geostrophic structure, minimizing variations in the direction of the rotation axis, and therefore reach through the whole fluid atmosphere. Lian and Showman (2008) show that even when the forcing is restricted to a shallow weather layer the jets may reach much deeper into the planet. Kaspi et al. (2009), on the other hand, present an anelastic deep convection model where the equatorial jet is geostrophic and

Email address: duarte@mps.mpg.de (Lúcia D. V. Duarte)

¹Max-Planck-Institut für Sonnensystemforschung

²Technische Universität Braunschweig

the higher latitude jets are confined to the outer few percent in radius.

Saturn’s magnetic field is very axisymmetric and shows a strong concentration towards the poles (Cao et al., 2012) which seems incompatible with a classical Earth like dynamo model. A stably stratified layer at the top of the dynamo region (Christensen and Wicht, 2008) or a completely different dynamo driven by differential rotation (Cao et al., 2012) are two alternatives to explain these features. We will therefore concentrate on comparisons with Jupiter’s field which is very similar to the geomagnetic field so that the well explored geodynamo models also seem to apply at first sight. These typically adopt the Boussinesq approximation where the mild density stratification of Earth’s core is simply ignored. Since this is certainly not justified in gas planets, some newer models therefore use the anelastic approximation which allows to incorporate the effects of the background density stratification while filtering out fast sound waves (Glatzmaier and Roberts, 1996; Stanley and Glatzmaier, 2010; Jones and Kuzanyan, 2009). In an extensive parameter study, Gastine et al. (2012) show that dipole-dominated dynamos are rather rare in anelastic models once larger density stratifications are assumed. We further discuss this analysis in section 3.

Ab initio calculations suggest that the electrical conductivity of the molecular envelope can not be neglected altogether (Lorenzen et al., 2011; French et al., 2012). Due to the increasing degree of hydrogen ionization the conductivity exponentially increases with depth and matches the conductivity of the metallic region at the transition radius without any pronounced jump. Because of the high temperatures beyond the critical point no clear transitions is discernable. The classical separation of the dynamics for the two envelopes thus becomes questionable. Liu et al. (2008) argue that this has important consequences for the depth of the zonal winds. These should remain confined to a shallow outer layer where the conductivity remains negligible. The strong shear associated with the zonal winds would otherwise create strong azimuthal magnetic field and lead to Ohmic heating incompatible with the observed luminosity (see however Glatzmaier, 2008).

Stanley and Glatzmaier (2010) present an anelastic simulation of a relatively thin shell with exponentially decaying electrical conductivity to model the very outer part of the shell. Dipole-dominated magnetic field develops in the presence of strong zonal winds reaching through the simulated region. Extreme parameters (i.e. low Ekman and Prandtl number and high Rayleigh number) were used but a detailed discussion and systematic parameter study to disentangle the effects of density stratification and varying conductivity are missing. Heimpel and Gómez Pérez (2011) also include a radial conductivity profile in their deep shell Boussinesq models, with a constant conductivity in the deeper interior and an exponential decay in the outer part. Once more well-pronounced deep-rooted zonal winds are compatible with dipole-dominated dynamo action.

The present paper extends the work of Gastine et al. (2012), that we will refer to as GDW12 in the following, by adding an electrical conductivity profile allowing to incorporate both the metallic and the molecular envelope. Following Heimpel

and Gómez Pérez (2011), the profile is loosely based on the *ab initio* calculations from French et al. (2012) with a constant conductivity in the metallic and an exponentially decaying conductivity in the molecular region. The aim is to explore under which circumstances strong zonal surface winds and dipole-dominated dynamo action can coexist.

In the next section, 2, we will describe the model with special attention to the anelastic formulation and the electrical conductivity profile. Section 3 presents the numerical results, first concentrating on the question of dipole-dominance and then on the dynamo mechanism. In the last section, 4, we summarize our main results and discuss their implication for the gas giants.

2. Model

2.1. Anelastic approximation

The fluid and convective interior of the planet is modelled by solving the MHD equations in a rapidly-rotating spherical shell. In the past, the Boussinesq approximation was typically used, which neglects the background density and temperature variations. This is questionable in gas planets and, following Gilman and Glatzmaier (1981), Braginsky and Roberts (1995) and Lantz and Fan (1999), we therefore adopt the anelastic approximation, where these background variations are now included but sound waves are ruled out by neglecting fast local density variations.

We solve the equations in a dimensionless form (Christensen and Aubert, 2006; Schrunner et al., 2012), using the shell thickness as a lengthscale ($d = r_o - r_i$, where r_o and r_i are the outer and inner radii of the spherical shell, respectively) and the viscous diffusion time as a timescale ($\tau_v = d^2/\nu$, where ν is the kinematic viscosity). Temperature and density are both non-dimensionalized by their values at the outer boundary, T_o and ρ_o . We employ constant entropy boundary conditions and use the imposed contrast across the shell as the entropy scale. There are no internal heat sources and all the heating coming into the shell via the inner boundary leaves it through the outer. While this is not the most realistic heating mode for gas giants, it has been chosen to ease the comparisons with more classical Boussinesq simulations. The magnetic field is scaled by $\sqrt{\mu\lambda\Omega\rho_o}$, where λ_i is the magnetic diffusivity at r_i , μ is the magnetic permeability and Ω is the frequency of rotation of the shell. The radial magnetic diffusivity profile $\lambda(r)$ is normalized by its value at the inner boundary, $\lambda_i = 1/(\sigma_i\mu)$, where σ_i is the electrical conductivity at r_i . The normalized magnetic diffusivity is $\tilde{\lambda} = \lambda(r)/\lambda_i = 1/(\tilde{\sigma}\mu)$.

The medium is assumed to be an electrically conducting ideal polytropic gas. Generally, dynamo simulations solve for small variations around an adiabatic hydrostatic background state that we mark with an overbar in the following. The temperature profile is then defined by the temperature gradient $d\bar{T}/dr = -g(r)/c_p$ and the density profile by $\bar{\rho}(r) = \bar{T}^m$, where m is the polytropic index. We assume a simple gravity profile proportional to radius, which assumes density roughly homogeneously distributed. The other extreme is to assume that all the mass is concentrated in the center, which leads to a gravity profile proportional to $1/r^2$ (Gilman and Glatzmaier, 1981; Jones

et al., 2011). Gastine et al. (2012) have shown that both gravity profiles lead to very similar results. The true profile of the gas giants lies somewhere in-between. The temperature reference state is then given by

$$\bar{T}(r) = -c_0 \left(\frac{r}{r_o} \right)^2 + 1 + c_0, \quad (1)$$

where

$$c_0 = 2 \frac{(e^{\frac{N_p}{m}} - 1)}{(1 - \eta^2)}. \quad (2)$$

$N_p = \ln(\rho_i/\rho_o)$ is the number of density scale heights between the inner and the outer boundaries of the shell and η is the ratio between the corresponding radii (see Jones et al., 2011; Gastine and Wicht, 2012, for the full derivation of the reference state).

The dimensionless form of the anelastic equations is then

$$E \left(\frac{\partial \mathbf{u}}{\partial t} + \mathbf{u} \cdot \nabla \mathbf{u} \right) = -\nabla \frac{p}{\bar{\rho}} - 2\mathbf{e}_z \times \mathbf{u} + \frac{Ra E}{Pr} \frac{r}{r_o} s \mathbf{e}_r + \frac{1}{Pm_i \bar{\rho}} (\nabla \times \mathbf{B}) \times \mathbf{B} + \frac{E}{\bar{\rho}} \nabla \cdot \mathbf{S}, \quad (3)$$

$$\frac{\partial \mathbf{B}}{\partial t} = \nabla \times (\mathbf{u} \times \mathbf{B}) - \frac{1}{Pm_i} \nabla \times (\tilde{\lambda} \nabla \times \mathbf{B}), \quad (4)$$

$$\bar{\rho} \bar{T} \left(\frac{\partial s}{\partial t} + \mathbf{u} \cdot \nabla s \right) = \frac{1}{Pr} \nabla \cdot (\bar{\rho} \bar{T} \nabla s) + \frac{Pr}{Ra} (1 - \eta) c_0 Q_v + \frac{Pr}{Pm_i^2 Ra E} (1 - \eta) c_0 Q_j, \quad (5)$$

$$\nabla \cdot (\bar{\rho} \mathbf{u}) = 0, \quad (6)$$

$$\nabla \cdot \mathbf{B} = 0, \quad (7)$$

where the traceless rate-of-strain tensor with constant kinematic viscosity is given by

$$\mathbf{S} = 2\bar{\rho} \left[\mathbf{e}_{ij} - \frac{1}{3} \delta_{ij} \nabla \cdot \mathbf{u} \right] \quad \text{and} \quad \mathbf{e}_{ij} = \frac{1}{2} \left(\frac{\partial u_i}{\partial x_j} + \frac{\partial u_j}{\partial x_i} \right), \quad (8)$$

where δ_{ij} is the identity matrix. The viscous and ohmic heating contributions are given by

$$Q_v = 2\bar{\rho} \left[\mathbf{e}_{ij} \mathbf{e}_{ji} - \frac{1}{3} (\nabla \cdot \mathbf{u})^2 \right], \quad (9)$$

$$Q_j = \tilde{\lambda} (\nabla \times \mathbf{B})^2, \quad (10)$$

The system of Eqs. (3–7) is governed by the dimensionless Ekman number, Rayleigh number, Prandtl number and magnetic Prandtl number, respectively,

$$E = \frac{\nu}{\Omega d^2}, \quad (11)$$

$$Ra = \frac{g_o d^3 \Delta s}{c_p \nu \kappa}, \quad (12)$$

$$Pr = \frac{\nu}{\kappa}, \quad (13)$$

$$Pm_i = \frac{\nu}{\lambda_i}, \quad (14)$$

where the thermal diffusivity κ , the specific heat c_p and the value of gravity at the outer radius, g_o , are constant.

2.2. Variable conductivity

To simulate the variable electrical conductivity of hydrogen in the interior of Jupiter, we employ a profile that corresponds to an approximately constant conductivity in the metallic hydrogen layer and an exponential decay in the outer molecular envelope. Both branches are matched via a polynomial that also ensures that the first radial derivative is continuous:

$$\tilde{\sigma}(r) = \begin{cases} 1 + (\tilde{\sigma}_m - 1) \left(\frac{r - r_i}{r_m - r_i} \right)^a & r < r_m \\ \tilde{\sigma}_m e^{a \left(\frac{r - r_m}{r_m - r_i} \right) \left(\frac{\tilde{\sigma}_m - 1}{\tilde{\sigma}_m} \right)} & r \geq r_m \end{cases}, \quad (15)$$

The exponential decay with a rate a starts at a radius r_m where the normalized conductivity has decreased from $\tilde{\sigma}_i = 1$ to $\tilde{\sigma}_m$. For convenience we also define the relative transition radius $\chi_m = r_m/r_o$ and we refer to it as a percentage.

This kind of profile has first been used by Gómez-Pérez et al. (2010) and it seems a fair first approximation to results from *ab initio* calculations (French et al., 2012). In our study, we mostly fix $\tilde{\sigma}_m$ to 0.5 and a to 9 while χ_m is varied from 95% to 70%. Since the decay rate is much too small when compared with the *ab initio* results, we also include a few cases with a much steeper decay of $a = 25$. Despite the very slow conductivity decay at $a = 9$, our results show no drastic changes and thus prove that this value seems sufficient to capture the main effects.

2.3. Numerical model

For the numerical simulation of the model described above, we use the anelastic version of the MagIC code (Wicht, 2002; Gastine and Wicht, 2012). This is a pseudo-spectral code that solves Eqs. (3–7) in a spherical shell using a poloidal/toroidal decomposition of the vector fields $\bar{\rho} \mathbf{u}$ and \mathbf{B} ,

$$\begin{aligned} \bar{\rho} \mathbf{u} &= (\bar{\rho} \mathbf{u})_{pol} + (\bar{\rho} \mathbf{u})_{tor} = \nabla \times (\nabla \times w \mathbf{e}_r) + \nabla \times z \mathbf{e}_r \\ \mathbf{B} &= \mathbf{B}_{pol} + \mathbf{B}_{tor} = \nabla \times (\nabla \times c \mathbf{e}_r) + \nabla \times a \mathbf{e}_r, \end{aligned} \quad (16)$$

where the scalar fields w , c are poloidal potentials and z , a are toroidal potentials. These potentials are then expanded in spherical harmonic functions up to degree and order l_{max} in latitudinal and longitudinal directions (θ and ϕ , respectively) and in Chebyshev polynomials in the radial direction (up to degree N_r).

For the parameter studies presented here, we use different resolutions, because the higher gradient in density and electrical conductivity demand an increase of both radial and horizontal resolution. The Chebyshev polynomials are truncated

from $N_r = 73$ to $N_r = 97$ and l_{max} ranges between 85 and 170. Each simulation ran for at least 1 magnetic diffusion time, except cases with lower Ekman number (see Tab. 2).

The boundary conditions for the velocity of our models are no slip at the inner core boundary and stress-free at the outer boundary. The stress-free outer boundary condition is more appropriate for a gas giant and allows for a more dynamical behaviour when compared with a rigid boundary (Simitev and Busse, 2009; Schrinner et al., 2012; Gastine et al., 2012). The existence of an inner core in Jupiter and its possible size (if it exists) is still unclear. Here we assume a small and conducting solid inner core with $r_i/r_o = 0.2$ (bigger than the model by Nettelmann et al., 2012, though), and we use a rigid flow boundary condition at the interface.

Furthermore, we use constant entropy boundary conditions, which means that we don't consider internal heat sources in our models. We match the magnetic field to a diffusive solution at the inner boundary and to a potential field at the outer boundary.

The Ekman number is either $E = 10^{-4}$ or $E = 10^{-5}$ for the simulations presented here. The relative moderate value of $E = 10^{-4}$ allows to more extensively scan the other system parameters like Rayleigh number, density stratification N_ρ and transition radius of the electrical conductivity profile χ_m . At $E = 10^{-5}$, we could only afford to run a few cases. We assume a Prandtl of $Pr = 1$ and magnetic Prandtl number at the inner boundary of $Pm_i = 2$ for $E = 10^{-4}$ and $Pm_i = 1$ for $E = 10^{-5}$.

Table 1: Values of critical Rayleigh number (Ra_{cr}) and critical wave number (m_{cr}) for each N_ρ . The values were obtained with a modified version of the linear code by Jones et al. (2009).

N_ρ	Ra_{cr}	m_{cr}	Ekman
0.0	8.706×10^5	4	10^{-4}
1.0	1.935×10^6	5	10^{-4}
2.0	3.455×10^6	6	10^{-4}
3.0	4.648×10^6	43	10^{-4}
4.0	4.569×10^6	49	10^{-4}
5.0	5.372×10^6	55	10^{-4}
5.5	6.172×10^6	58	10^{-4}
0.0	2.073×10^7	9	10^{-5}
1.0	4.498×10^7	11	10^{-5}
2.0	5.582×10^7	11	10^{-5}
3.0	1.026×10^8	11	10^{-5}
3.5	1.130×10^8	92	10^{-5}

All together, we simulated 50 cases in a range of 4 to 46 times supercritical. Gastine and Wicht (2012) examined anelastic convection for an aspect ratio of 0.6 and showed that the critical Rayleigh number increases with increasing stratification N_ρ . Table 1 demonstrates that we observe a similar trend for the smaller aspect ratio 0.2 employed here. At a certain stratification the wave number jumps from lower to high values. This is the point where the onset of convection moves from the inner to the outer boundary (Gastine and Wicht, 2012). The transition is delayed for the lower Ekman number (see also Jones et al., 2009).

We consider a polytropic index of $m = 2$ in our anelastic sim-

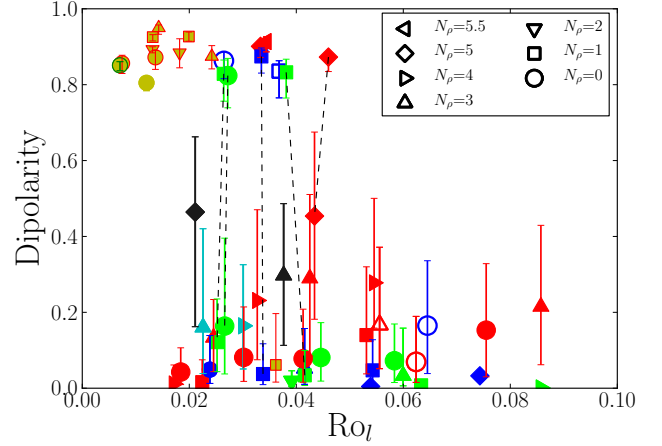


Figure 1: Dipolarity against the local Rossby number calculated only for the conducting region (Eq. 21). Colour corresponds to different transition radii: cyan – $\chi_m = 70\%$, red – $\chi_m = 80\%$, blue – $\chi_m = 90\%$, green – $\chi_m = 95\%$. The open symbols are cases with a no slip upper boundary, instead of stress-free. The error bars correspond to standard deviations of the time series of each case, for which the point itself is the time average. The cases in black color correspond to $a = 25$ and $\chi_m = 80\%$. The three dashed lines connect three sets of cases for which we found two solutions, depending on the initial magnetic field. The cases indicated in dark yellow outlined in red (green) correspond to $E = 10^{-5}$ simulations with $\chi_m = 80\%$ ($\chi_m = 95\%$). Finally the yellow symbol without the red line is the case from Heimpel and Gómez Pérez (2011) of $\chi_m = 80\%$ and $\eta = 0.35$.

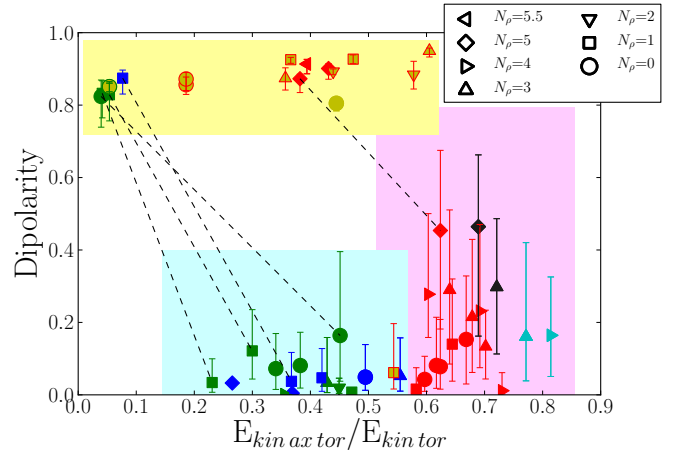


Figure 2: Dipolarity plotted against the ratio between the toroidal kinetic energy and the total kinetic energy, averaged in time and volume. The symbols have the same definition as in Fig. 1. The three boxes mark the three different regimes discussed in the text. The three dashed lines connect three sets of cases for which we found two solutions, depending on the initial magnetic field.

ulations. The explored density scale heights range from the Boussinesq case $N_\rho = 0$ to $N_\rho = 5.5$ which corresponds to a density jump of $\rho_i/\rho_o \simeq 245$. *Ab initio* simulations suggest a Jovian stratification of $N_\rho = 8.5$ ($\rho_i/\rho_o \simeq 5000$) from the bottom of the molecular hydrogen layer to the 1 bar level (Guillot, 1999; French et al., 2012). However this is mostly concentrated

in the outermost 1% and our largest stratification indeed covers 99% of the planet.

2.4. Diagnostic parameters

The parameters of all the numerical experiments discussed here are listed in Tab. 2 along with several quantities that characterize the solution. The amplitude of the zonal axisymmetric flow component is measured in terms of the Rossby number Ro_{zon} :

$$Ro_{zon} = \frac{u_{zon}}{\Omega d}, \quad \text{with} \quad u_{zon} = \sqrt{\frac{1}{V} \int_{r_i}^{r_o} \langle u_{tor, m=0}^2 \rangle r^2 dr}, \quad (17)$$

where the triangular brackets denote the angular average

$$\langle f \rangle = \frac{1}{4\pi} \int_0^\pi \int_0^{2\pi} f(r, \theta, \phi) \sin\theta d\theta d\phi \quad (18)$$

and V is the volume of the spherical shell. The magnetic Reynolds number estimates the ratio of magnetic field production and diffusion. We use a modified form to account for the radial-dependent magnetic diffusivity,

$$R_m = \frac{3}{r_o^3 - r_i^3} \int_{r_i}^{r_o} \frac{\sqrt{\langle u^2(r, \theta, \phi) \rangle}}{\lambda(r)} r^2 dr. \quad (19)$$

The local Rossby number has been introduced by [Christensen and Aubert \(2006\)](#) to quantify the relative importance of the advection term in the Navier-Stokes equation (Eq. 3):

$$Ro_\ell = \frac{\sqrt{\frac{1}{V} \int_{r_i}^{r_o} \langle u^2 \rangle r^2 dr}}{\Omega \ell}. \quad (20)$$

Here, we use a modified version of Ro_ℓ calculated only for the inner conducting region ($r_i \leq r \leq r_m$),

$$Ro_\ell = \frac{3}{r_o^3 - r_i^3} \int_{r_i}^{r_m} \frac{\sqrt{\langle u^2(r, \theta, \phi) \rangle}}{\Omega \ell(r)} r^2 dr, \quad (21)$$

where ℓ is the mean flow length scale given by

$$\ell(r) = \frac{\pi u^2(r)}{\sum_l l u_l^2(r)}, \quad (22)$$

with u_l the flow contribution of spherical harmonic degree l .

The magnetic field strength is quantified by the Elsasser number which measures the ratio of Lorentz to Coriolis forces using the modified form

$$\Lambda = \frac{1}{\mu_0 \Omega V} \int_{r_i}^{r_o} \left\langle \frac{\mathbf{B}^2}{\rho(r) \lambda(r)} \right\rangle r^2 dr. \quad (23)$$

The geometry of the surface field is characterized by its dipolarity

$$Dipolarity = \frac{\langle (\mathbf{B}_{l=1}^{m=0})^2 \rangle}{\left\langle \sum_{l,m \leq 12} (\mathbf{B}_l^m)^2 \right\rangle}, \quad (24)$$

which measures the relative energy in the axial dipole contribution at the outer boundary r_o . Following [Christensen and Aubert \(2006\)](#), we restricted the magnetic field to spherical harmonic degrees and orders below 12 in Eq. 24. The time variability of dipolarity is quantified by its standard deviation SD_{dip} shown in Tab. 2.

The properties described in this section are referred in Tab. 2 by their time averages.

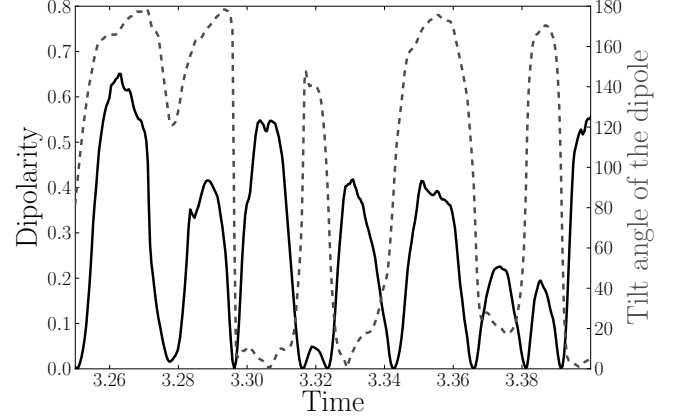


Figure 3: Time evolution of the dipolarity at the surface (solid black line) and the tilt angle of the dipole (dashed grey line) in degrees. The time is given in magnetic diffusion units. The parameters are: $E = 10^{-4}$, $N_\rho = 3$, $Ra = 4.3 Ra_{cr}$, $\chi_m = 80\%$.

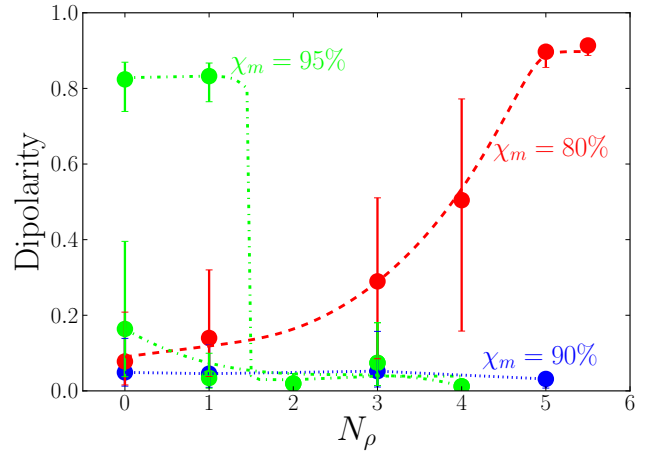


Figure 4: Dipolarity against density stratification, for fixed transition radii: red - $0.8 r_o$, blue - $0.9 r_o$, green - $0.95 r_o$. The dashed lines simply gather the symbols with the same χ_m . The error bars are the same as in Fig. 1. The $\chi_m = 70\%$ cases were excluded, since we didn't find dipolar solutions up to now.

3. Results

Before presenting the new simulations for a radial conductivity profile, we briefly summarize the main findings of GDW12. They explored the effects of density stratification on numerical

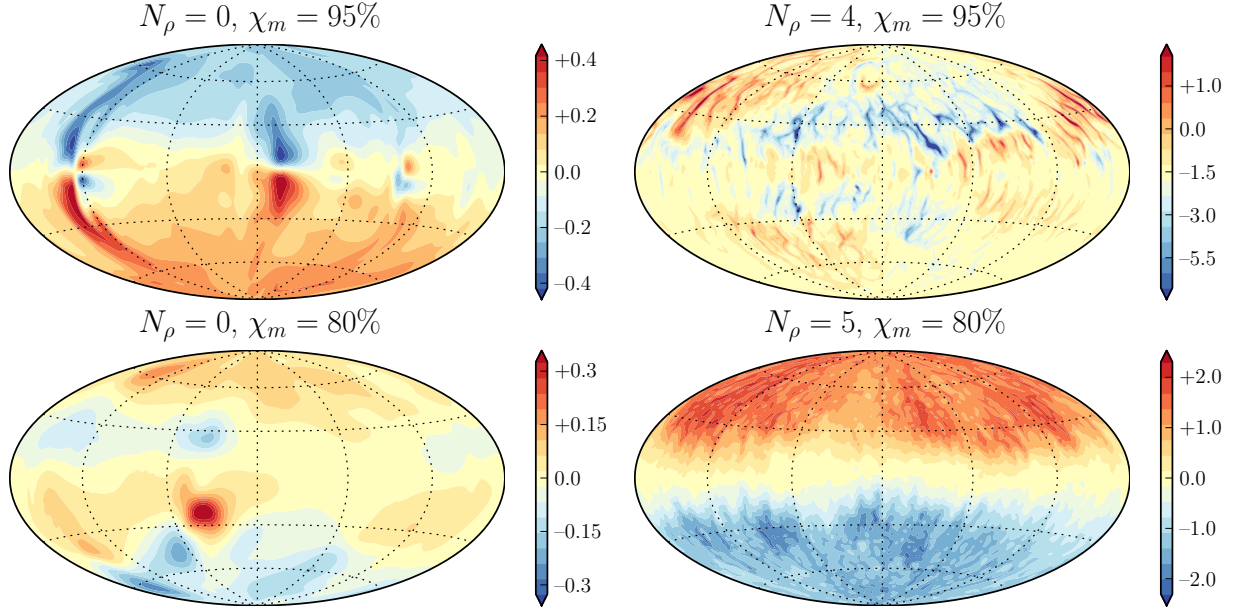


Figure 5: Radial magnetic field at the outer boundary. The top row corresponds to $\chi_m = 95\%$ (cases 9d and 33 of Tab. 2, respectively) and the bottom row to $\chi_m = 80\%$ (cases 3 and 34 of the same table). The maps on the left are $N_\rho = 0$ cases and the maps on the right column are $N_\rho = 4$ (top) and $N_\rho = 5$ (bottom). Magnetic fields are given in units of Elsasser number.

dynamo simulations with homogeneous electrical conductivity, focussing mainly on the question of magnetic field geometry. Ekman and Prandtl numbers are identical to most of the cases explored here. The stratification was varied up to $N_\rho = 3$ and two different aspect ratios, $\eta = 0.2$ and $\eta = 0.6$, were explored with very similar results.

For the smaller to intermediate stratifications $N_\rho \leq 2$, only multipolar magnetic fields were found when the local Rossby number exceeds about $Ro_\ell \approx 0.1$. This confirmed the findings of Christensen and Aubert (2006) who introduced the Ro_ℓ to separate dipole-dominated from multipolar dynamo simulations in their Boussinesq models.

Below $Ro_\ell \approx 0.1$, GDW12 find a bistable regime where multipolar and dipole-dominated solutions coexist and form two distinct branches. This bistability can likely be attributed to the fact that stress-free boundary conditions were employed (Simitev and Busse, 2009; Schinnerer et al., 2012; Gastine et al., 2012). For rigid conditions, only the dipolar branch seems to exist. Stress-free boundary conditions allow strong zonal winds to develop that compete with large scale magnetic fields. On the dipolar branch zonal winds are weak, on the multipolar branch they are stronger.

For larger density stratifications, $N_\rho > 2$, no dipole-dominated solutions were found. This was attributed to the fact that the focus of convective action moves progressively outward when the stratification is increased. When convective columns are mainly confined to a thin region close to the outer boundary, a new non-axisymmetric dynamo mode is preferred that has previously been observed in some mean field dynamo simulations (Rüdiger et al., 2003; Jiang and Wang, 2006).

3.1. Dynamo regimes

We start with discussing the different dynamo regimes based on the $E = 10^{-4}$ cases and come back to $E = 10^{-5}$ solutions in section 3.3. Our new results for depth-dependent conductivity are subsumed in Figs. 1 and 2. Figure 1 displays the time-averaged dipolarity at the outer boundary versus the time-averaged local Rossby number calculated for the metallic hydrogen region only ($r/r_o < \chi_m$).

Figure 2 shows the time-averaged dipolarity versus the relative time-averaged zonal wind energy. Three distinct groups of solutions can be identified.

When the weakly conducting layer is thin ($\chi_m = 95\%$ and $\chi_m = 90\%$) we largely recover the results from GDW12: for weak stratification and $Ro_\ell \leq Ro_{\ell c}$, there are two branches with either weak dipolarity and stronger zonal flows (cyan area in Fig. 2) or strong dipolarity and weaker zonal flows (green and blue symbols inside the yellow area in Fig. 2). Our results also agree with the findings by Christensen and Aubert (2006) in the sense that above a critical local Rossby number value $Ro_{\ell c}$ only multipolar solutions can be found. However, the value of Ro_ℓ is significantly decreased from 0.1 to about 0.045. This is consistent with Gómez-Pérez et al. (2010) who reported that introducing a thin weakly conducting layer in a dipole-dominated dynamo model resulted in a multipolar solution. The aspect ratio has an additional but milder effect on the transitional Ro_ℓ value which is reduced for smaller inner cores.

When the thickness of the weakly conducting layer is increased, we also find two distinct types of solutions: a new group of very time-dependent solutions (the pink area in Fig. 2) and a group of solutions with more stable strongly dipolar fields (within the yellow area). The latter results from combining a strong stratification (diamonds, $N_\rho = 5$ and left-triangles,

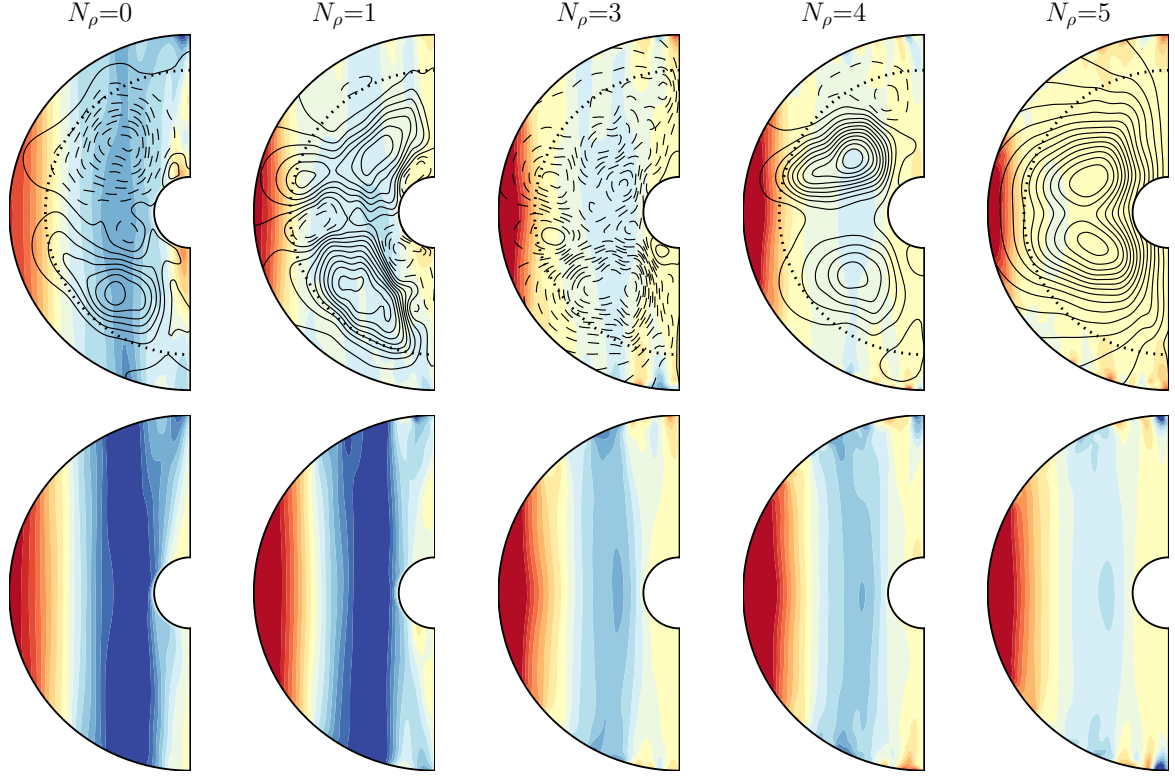


Figure 6: Azimuthal averages of the zonal component of the flow. Each column of two plots has a different N_ρ , namely 0, 1, 3, 4 and 5 from left to right. In the top row, the poloidal fieldlines are plotted on top of the zonal velocity contours, where solid lines are positive values and dashed are negative values. The dotted line corresponds to the transition $r_m = 80\%$. The bottom row shows the corresponding hydrodynamical solutions (i.e. without magnetic field). All cases have the same contour levels (the red corresponds to prograde and the blue to retrograde, the maximum and minimum values are 0.05 and -0.05 , respectively, in units of Rossby number determined by $Ro = u/(\Omega r_o)$).

$N_\rho = 5.5$) with a thicker weak conductivity layer (red colored symbols, $\chi_m = 80\%$).

The new oscillatory solutions promoted by the more pronounced weak conductivity layer (red, $\chi_m = 80\%$ and cyan, $\chi_m = 70\%$) are indicated by large error bars (within the pink box in Fig. 2), measuring the standard deviation around the time-averaged dipolarity. Figure 3 demonstrates that this strong time dependence results from the fact that these cases oscillate between dipolar and multipolar solutions. When the dipole is weak, it can significantly tilt away from the rotation axis and even undergo polarity reversals.

3.2. Competition between zonal flows and magnetic field

Figure 4 highlights the role of the density stratification at $E = 10^{-4}$. When the weakly conducting layer has a negligible influence, dipole-dominated solutions can only be found for $N_\rho < 2$, as well as bistability (Y shape of the green dashed line). For thicker and thus influential layers, however, the mean dipolarity increases with stratification. For low to intermediate N_ρ , oscillatory cases, similar to the case displayed in Fig. 3, are found. For larger stratifications they finally settle into the very strongly dipolar and more stable solutions.

Snapshots of the radial magnetic field at $E = 10^{-4}$ at the outer boundary illustrate the different type of solutions in Fig. 5. The top row shows a dipole-dominated Boussinesq case and

the multipolar solution caused by a strong density stratifications (see GDW12). Note that the field presents a wavy structure ($m=1$) typical for this multipolar dynamos with stress-free boundaries (Goudard and Dormy, 2008, GDW12). The weakly conducting layer is only thin here with $\chi_m = 95\%$ and has negligible influence on the dynamo action. The second row depicts the new solution branches found for $\chi_m = 80\%$. The left panel shows a snapshot of a Boussinesq multipolar case and the right panel illustrates the dipolar configuration found at strong stratifications. At the equator, the dipole field is reduced in the $N_\rho = 5$ cases.

Why does the combination of a thicker weakly conducting outer layer and a strong stratification help to get dipole-dominated solutions? We recall that GDW12 found two reasons why the dynamo process prefers to produce multipolar fields: for one, there is a competition between strong zonal jets and larger scale magnetic fields, and second, stronger stratifications confine the dominant convective features to a thin outer layer where they tend to produce non-axisymmetric field. We had the hope that introducing the weakly conducting layer alone would promote dipolar dynamo action, allowing zonal winds to develop in the outer layer while dipolar dynamo action takes place in the deeper interior (Stanley and Glatzmaier, 2010; Heimpel and Gómez Pérez, 2011).

The top row of Fig. 6 illustrates how the zonal flow and

the poloidal magnetic field change when increasing the density stratification in a case with a pronounced weakly conducting layer ($\chi_m = 80\%$) and the bottom row shows the corresponding non-magnetic cases. In the latter, increasing density stratification has very significant effect on the retrograde jet, which gradually disappears and is mostly gone at $N_\rho = 5$. This shows that increasing N_ρ reduces drastically the amplitude of the zonal flows in the conducting part, where the dynamo is generated. This asymmetry between prograde and retrograde jets is typical for anelastic models with stress-free boundaries and strong density stratifications. For $N_\rho = 0$, the typical three jet structure develops with a strong prograde equatorial jet and two flanking retrograde jets at higher latitudes (Gastine and Wicht, 2012). These flows still have a geostrophic structure and they penetrate the whole shell, in a similar way as the corresponding hydrodynamic solution. The competition between dipolar fields and zonal flows leads to the oscillatory solution type (pink area in Fig. 2) where either the dipolar field or the zonal flows are strong. The remaining prograde jet completely resides within the weak conductivity envelope so that the zonal flow/dipole competition is not an issue any more. The same is true for the confined convective features that additionally promote non-axisymmetric magnetic fields at larger stratifications.

The poloidal magnetic field is now produced by convection residing deeper in the shell. This is illustrated by Fig. 7 showing the radial profiles of poloidal and toroidal magnetic energies for the five solutions depicted in Fig. 6. Up to a stratification of $N_\rho = 4$, poloidal and toroidal energies have similar profiles and peak in the outer part of the conducting region. For $N_\rho = 5$, however, the profiles are different with a pronounced focus on deeper parts of the shell. For $N_\rho \leq 4$ the toroidal field is larger than the poloidal, suggesting that the induction mechanism is different from the dipole-dominated cases where the poloidal field is stronger.

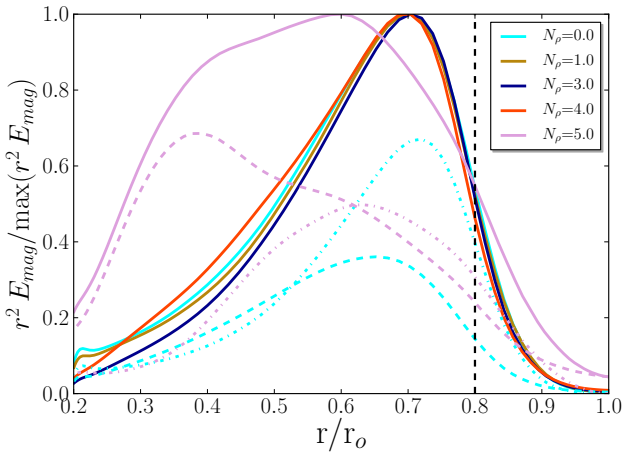


Figure 7: Radial profile of magnetic energy flux ($r^2 E_{mag}$) averaged over time. The dashed black line is the location of $\chi_m = 80\%$. These results correspond to the red triangles and red dashed line from Fig. 4. The poloidal (dashed lines) and toroidal (dot-dashed lines) components are also shown for $N_\rho = 5$ and $N_\rho = 0$, with the corresponding colours. The magnetic energy fluxes are normalized by their maximum values.

Gastine et al. (2012) have reported that the multipolar solutions with stronger zonal flows are dynamos of $\alpha\Omega$ or $\alpha^2\Omega$ type. The Ω stands here for the production of toroidal field by global zonal wind shear while α stands for poloidal and toroidal field production by more local helical structures. It is difficult to differentiate whether the importance of the Ω -effect is a reason for the multipolar nature of these solutions or arises because the large scale Lorentz forces tied to dipolar field contributions are missing.

Following Brown et al. (2011), the Ω -effect is given by

$$\Omega = \overline{B_r}^\phi \frac{\partial}{\partial r} \left(\frac{\overline{u_\phi}^\phi}{r} \right) + \frac{\overline{B_\theta}^\phi \sin \theta}{r} \frac{\partial}{\partial \theta} \left(\frac{\overline{u_\phi}^\phi}{\sin \theta} \right), \quad (25)$$

and the mean ohmic diffusion (MD – mean diffusion) by

$$\text{MD} = \eta \nabla^2 \overline{B_\phi}^\phi - \frac{\eta \overline{B_\phi}^\phi}{r^2 \sin^2 \theta} + \frac{d\eta}{dr} \left(\frac{1}{r} \frac{\partial (r \overline{B_\phi}^\phi)}{\partial r} \right), \quad (26)$$

where the overbars correspond to zonal averages. Figure 8 displays the axisymmetric azimuthal toroidal field along with the Ω -effect and the respective mean Ohmic diffusion for the $N_\rho = 3$ and the $N_\rho = 5$ solutions already depicted in Figs. 6 and 7. For the multipolar solution at $N_\rho = 3$, the Ω -effect plays an important role as demonstrated by the high degree of correlation with the azimuthal field over the shell. For the dipole-dominated solution at $N_\rho = 5$, however, the Ω -effect is only strong in the weakly conducting region where it is effectively balanced by the mean diffusion. The dynamo mechanism thus changes from $\alpha\Omega$ or $\alpha^2\Omega$ to α^2 at stronger stratification. Dynamos of the latter type are known to produce dipole-dominated magnetic fields (Olson et al., 1999).

3.3. Ekman number 10^{-5}

The Boussinesq results by Heimpel and Gómez Pérez (2011) suggest that the competition between zonal flows and dipolar field may be less severe at the lower Ekman number 10^{-5} they employed. To explore this, we added eleven simulations at $E = 10^{-5}$ and different Rayleigh numbers and stratifications, adopting the transition radius $\chi_m = 80\%$ and one case of $\chi_m = 95\%$. Note that one Boussinesq case is identical to one of the models presented by Heimpel and Gómez Pérez (2011) (case 50 in Tab. 2). Yellow symbols indicate these runs in both Figs. 1 and 2.

Having values of Ro_ℓ around 0.01–0.02 and high dipolarity they are located on the left side of the dipole-multipole transition in Fig. 1. At $Ro_\ell \approx 0.035$ and $N_\rho = 1$, there is case which has higher value of Rossby number and it is multipolar, as expected. Unlike for the larger Ekman number of $E = 10^{-4}$, even Boussinesq or mildly stratified solutions are now dipole-dominated and fall into the yellow regime outlined in Fig. 2. They are also very stable in time.

Figure 9 compares two $E = 10^{-5}$ solutions at $N_\rho = 1$ and $N_\rho = 3$ with the $N_\rho = 5$ and $E = 10^{-4}$ model already shown in Fig. 6. The field is clearly strongly dipolar in all cases, there are pronounced equatorial jets and much weaker retrograde jets at higher latitudes; both aspects were already reported by Heimpel and Gómez Pérez (2011) for their Boussinesq model. At

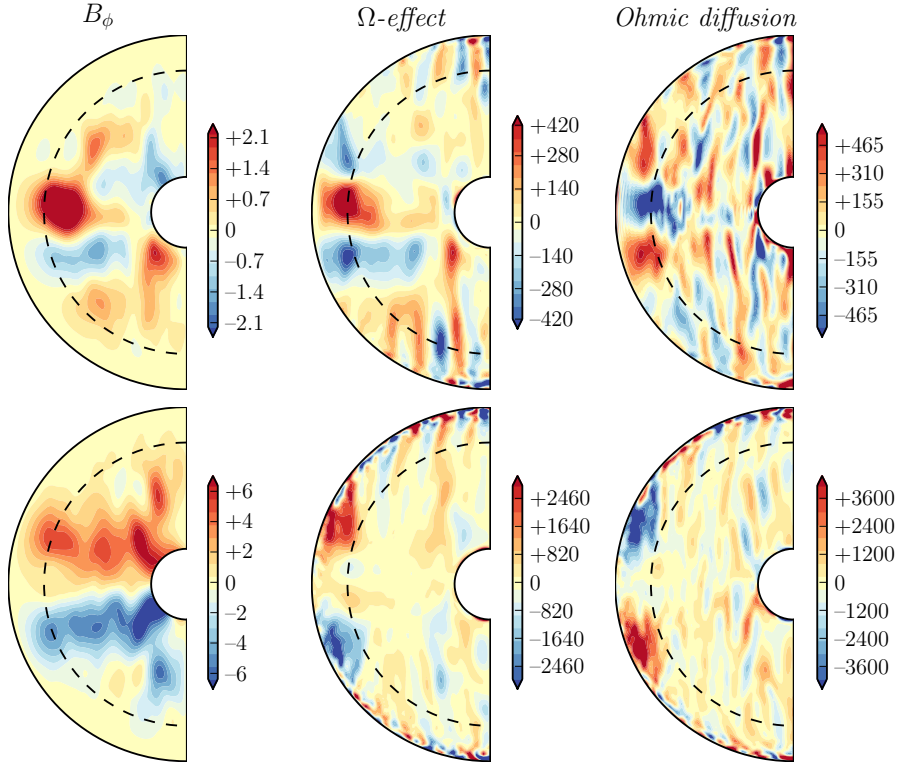


Figure 8: From left to right, azimuthal averages of the toroidal component of the magnetic field, production of the toroidal field by Ω -effect and ohmic diffusion. The three upper panels correspond to $N_\rho = 3$, $Ra = 2 \times 10^7$ and the three lower panels to $N_\rho = 5$, $Ra = 4 \times 10^7$, both cases belong to the red line of Fig. 4.

both Ekman numbers, the relative amplitude of the retrograde jets decreases with N_ρ . Note, however, that the amplitude of the dominant equatorial jet is significantly smaller in all lower Ekman number cases. For example, the zonal flow Rossby number is $Ro_{zon} = 9.8 \times 10^{-4}$ in the ($E = 10^{-5}$, $N_\rho = 1$) case depicted in Fig. 9 but $Ro_{zon} = 8.0 \times 10^{-3}$ in the ($E = 10^{-4}$, $N_\rho = 5$) simulation. The peak surface velocity of the equatorial jet is around $Ro_{ej} = 4.8 \times 10^{-2}$ for Jupiter (Vasavada and Showman, 2005) and the $E = 10^{-4}$ simulations come much closer to this value than the $E = 10^{-5}$ cases. The ($E = 10^{-4}$, $N_\rho = 5$) case illustrated in Fig. 9 reaches indeed $Ro_{ej} = 5.3 \times 10^{-2}$ compared to $Ro_{ej} = 3.7 \times 10^{-3}$ for the ($E = 10^{-5}$, $N_\rho = 1$) example.

The slower jet speeds at the lower Ekman number are not caused by Lorentz forces but are already present in the non-magnetic simulations. In order to reach more realistic flow amplitudes at $E = 10^{-5}$ the Rayleigh number needs to be increased. According to Heimpel and Gómez Pérez (2011), however, this would once more lead to multipolar magnetic fields. The larger jet speed reached in the ($E = 10^{-5}$, $N_\rho = 3$) case shown in Fig. 9 suggests that increasing the stratification may once more help here to retain dipolar dynamo action in the presence of stronger equatorial jets. For weak stratification the principle difficulty of consolidating strong zonal winds and dipole dominated fields remains an issue at the lower Ekman number.

Elsasser number and magnetic Reynolds number are comparable in our dipole-dominated $E = 10^{-4}$ cases of $N_\rho \geq 5$ with thicker outer low-conductivity layers and the $E = 10^{-5}$ cases (see Tab. 1). The Elsasser number is a measure for the ratio of Lorentz to Coriolis forces in the Navier-Stokes equation, while the magnetic Reynolds number quantifies the ratio of magnetic induction to diffusion in the dynamo equation. Similar force balance and magnetic balance thus seems to hold at both Ekman numbers with zonal flows playing only a minor role in these dominantly α^2 -dynamos. For a more detailed analyses we refer to Heimpel and Gómez Pérez (2011).

4. Discussion and conclusions

We have studied dynamo simulations with a conductivity profile geared to model the dynamics of the metallic and the molecular envelopes of the gas giants in one simulation. The goal was to find strong zonal surface jets along with dipole-dominated dynamo action which is difficult when the electrical conductivity is homogeneous (Gastine et al., 2012). The solutions then either have strong zonal winds and multipolar magnetic fields or weak zonal winds and dipole-dominated magnetic fields. Sometimes bistability is found where both types of solutions coexist at the same parameters.

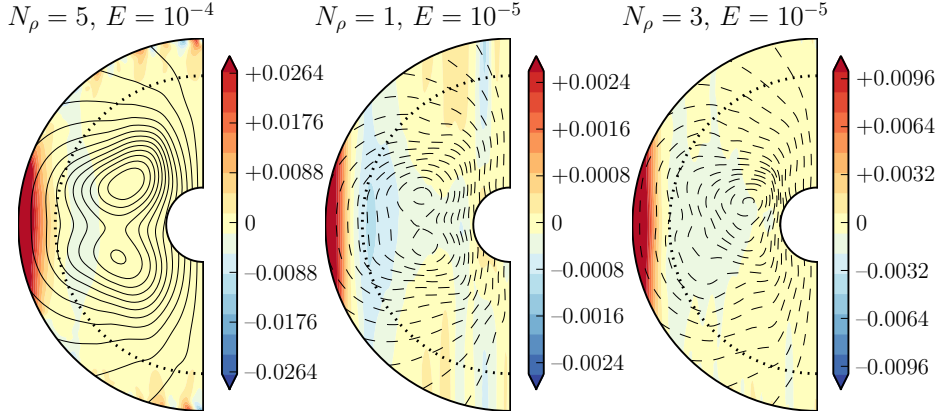


Figure 9: Azimuthal average of the zonal component of the flow. The parameters are: $E = 10^{-5}$, $\chi_m = 80\%$, $Ra = 4.4 Ra_{cr}$ for $N_\rho = 1$ and $Ra = 3.9 Ra_{cr}$ for $N_\rho = 3$. The poloidal fieldlines are plotted on top of the zonal velocity contours, where solid lines are positive and dashed are negative values. The dotted lines correspond to $r_m = 80\%$. Zonal velocities are given in units of Rossby number calculated by $Ro = u/(\Omega r_o)$.

Even thin weakly conducting outer layers already have an effect on the dynamo process (Gómez-Pérez et al., 2010) and reduce the window where dipole-dominated dynamo solutions can be found at mild stratifications. The local Rossby number that marks the transition between dipolar and multipolar cases reduces from $Ro_\ell \approx 0.1$ to $Ro_\ell \approx 0.03$ at $\chi_m = 95\%$. The zonal flows remain weak in some of these cases and the reason for the loss of dipolar dominance remains unclear. Gómez-Pérez et al. (2010) speculate that the separation of the Ekman and Hartmann boundary layers may play a role.

A sizable weakly conducting outer layer ($\chi_m = 80\%$) allows stronger zonal winds to develop and the competition with the dipolar field becomes even more problematic than in simulations with homogeneous conductivity. When the stratification is weak, only multipolar solutions remain where dipole-dominated solutions could still be found for homogeneous conductivity. This changes, however, when the stratification is increased at $E = 10^{-4}$. At intermediate values, the solutions become highly time dependent, oscillating between dipolar and multipolar configurations. At strong stratifications, highly dipolar and stable solutions are found. The main reason likely is that for the strongly stratified cases explored here the fierce equatorial jet is confined to the weakly conducting outer region introduced to model the molecular envelope. The flanking retrograde jets, however, that cover the higher conducting inner region where the main dynamo action takes place, remain weak. For lower Ekman numbers, dipole-dominated solutions are also obtained at lower density stratifications. These solutions present weaker zonal jets, similarly to previous Boussinesq studies by Heimpel and Gómez Pérez (2011).

Compared to Jupiter or Saturn there are too few zonal jets in our simulations. Also, the strong decrease in amplitude from equatorial to flanking jets necessary to retain dipolar dynamo action is not compatible with the observations, at least for Jupiter. Dipolar dynamo action could nevertheless be retained for Jupiter if the higher latitude jets were too shallow to become important for the dynamo process.

Another argument against deep reaching winds is that the as-

sociated strong Ω -effect and Ohmic dissipation may also not be compatible with Jupiter's observed luminosity (Liu et al., 2008). First analysis of our results confirm that the Ω -effect and associated Ohmic dissipation can be significant. However, as Glatzmaier (2008) argues, the magnetic field may assume a configuration that minimizes the efficiency of the Ω -effect. Magnetic fieldlines tend to remain perpendicular to the flow shear which minimizes Lorentz forces and also the Ω -effect. Fig. 9 illustrates that the magnetic fieldlines indeed tend to be aligned with the rotation axis in the outer part of the shell to remain perpendicular to the strong shear where electrical conductivity is still sizable. This helps to minimize Ohmic dissipation which nevertheless remains significant in all our simulations with strong zonal flows. Further investigation are necessary to quantify this effect and extrapolate it to the planetary situation.

Any problems related to Ohmic dissipation and dipolar dynamo action would be solved if the main zonal jets were confined to a thin outer envelope where the electrical conductivity is negligible (Liu et al., 2008). In our simulations all the stronger jets obey the Taylor-Proudman theorem and reach through the planet. Shallow jets have been found by Kaspi et al. (2009), however, who use a different anelastic approximation and a different internal heating mode. Further investigations are required to clarify which specific model features influences the depth on the zonal jets.

Acknowledgements

All the computations have been carried out on the GWDG computer facilities in Göttingen and in the Max-Planck-Institut für Sonnensystemforschung. This work was supported by the Special Priority Program 1488 (PlanetMag, <http://www.planetmag.de>) of the German Science Foundation.

References

- Braginsky, S. I., Roberts, P. H., 1995, Equations governing convection in earth's core and the geodynamo. *Geophysical and Astrophysical Fluid Dynamics* 79, 1-97.

- Brown, B. P., Miesch, M. S., Browning, M. K., Brun, A. S., Toomre, J., 2011, Magnetic Cycles in a Convective Dynamo Simulation of a Young Solar-type Star. *Astrophysical Journal* 731, 69.
- Cao, H., Russell, C. T., Wicht, J., Christensen, U. C., Dougherty, M. K., Aug. 2012, Saturn's High Degree Magnetic Moments: Evidence for a Unique Planetary Dynamo. *Icarus*, in press.
- Chabrier, G., Saumon, D., Hubbard, W. B., Lunine, J. I., Jun. 1992, The molecular-metallic transition of hydrogen and the structure of Jupiter and Saturn. *Astrophysical Journal* 391, 817-826.
- Cho, J. Y.-K., Polvani, L. M., Jul. 1996, The Morphogenesis of Bands and Zonal Winds in the Atmospheres on the Giant Outer Planets. *Science* 273, 335-337.
- Christensen, U. R., Nov. 2002, Zonal flow driven by strongly supercritical convection in rotating spherical shells. *Journal of Fluid Mechanics* 470, 115-133.
- Christensen, U. R., Aubert, J., Jul. 2006, Scaling properties of convection-driven dynamos in rotating spherical shells and application to planetary magnetic fields. *Geophysical Journal International* 166, 97-114.
- Christensen, U. R., Wicht, J., Jul. 2008, Models of magnetic field generation in partly stable planetary cores: Applications to Mercury and Saturn. *Icarus* 196, 16-34.
- Fortney, J. J., Nettelmann, N., May 2010, The Interior Structure, Composition, and Evolution of Giant Planets. *Space Science Reviews* 152, 423-447.
- French, M., Becker, A., Lorenzen, W., Nettelmann, N., Bethkenhagen, M., Wicht, J., Redmer, R., Sep. 2012, Ab Initio Simulations for Material Properties along the Jupiter Adiabatic. *Astrophysical Journal, Supplement* 202, 5.
- Gastine, T., Duarte, L., Wicht, J., Oct. 2012, Dipolar versus multipolar dynamos: the influence of the background density stratification. *Astronomy and Astrophysics* 546, A19.
- Gastine, T., Wicht, J., May 2012, Effects of compressibility on driving zonal flow in gas giants. *Icarus* 219, 428-442.
- Gilman, P. A., Glatzmaier, G. A., Feb. 1981, Compressible convection in a rotating spherical shell. I - Anelastic equations. II - A linear anelastic model. III - Analytic model for compressible vorticity waves. *Astrophysical Journal, Supplement* 45, 335-388.
- Glatzmaier, G. A., Roberts, P. H., Oct. 1996, An anelastic evolutionary geodynamo simulation driven by compositional and thermal convection. *Phys. D* 97 (1-3), 81-94.
- Glatzmaier, G. A., Aug. 2008, A note on "Constraints on deep-seated zonal winds inside Jupiter and Saturn". *Icarus* 196, 665-666.
- Gómez-Pérez, N., Heimpel, M., Wicht, J., Jul. 2010, Effects of a radially varying electrical conductivity on 3D numerical dynamos. *Physics of the Earth and Planetary Interiors* 181, 42-53.
- Goudard, L., Dormy, E., Sep. 2008, Relations between the dynamo region geometry and the magnetic behavior of stars and planets. *EPL (Europhysics Letters)* 83, 59001.
- Guillot, T., Oct. 1999, Interior of Giant Planets Inside and Outside the Solar System. *Science* 286, 72-77.
- Heimpel, M., Aurnou, J., Wicht, J., Nov. 2005, Simulation of equatorial and high-latitude jets on Jupiter in a deep convection model. *Nature* 438, 193-196.
- Heimpel, M., Gómez Pérez, N., Jul. 2011, On the relationship between zonal jets and dynamo action in giant planets. *Geophysics Research Letters* 38, 14201.
- Ingersoll, A. P., Beebe, R. F., Collins, S. A., Mitchell, J. L., Terile, R. J., Hunt, G. E., Muller, P., Smith, B. A., Aug. 1979, Zonal velocity and texture in the Jovian atmosphere inferred from Voyager images. *Nature* 280, 773-775.
- Jiang, J., Wang, J.-X., Apr. 2006, A Non-axisymmetric Spherical α^2 -Dynamo. *Chinese Journal of Astronomy and Astrophysics* 6, 227-236.
- Jones, C. A., Boronski, P., Brun, A. S., Glatzmaier, G. A., Gastine, T., Miesch, M. S., Wicht, J., Nov. 2011, Anelastic convection-driven dynamo benchmarks. *Icarus* 216, 120-135.
- Jones, C. A., Kuzanyan, K. M., Mitchell, R. H., Aug. 2009, Linear theory of compressible convection in rapidly rotating spherical shells, using the anelastic approximation. *Journal of Fluid Mechanics* 634, 291.
- Jones, C. A., Kuzanyan, K. M., Nov. 2009, Compressible convection in the deep atmospheres of giant planets. *Icarus* 204, 227-238.
- Kaspi, Y., Flierl, G. R., Showman, A. P., Aug. 2009, The deep wind structure of the giant planets: Results from an anelastic general circulation model. *Icarus* 202, 525-542.
- Lantz, S. R., Fan, Y., Mar. 1999, Anelastic Magnetohydrodynamic Equations for Modeling Solar and Stellar Convection Zones. *Astrophysical Journal, Supplement* 121, 247-264.
- Lian, Y., Showman, A. P., Apr. 2008, Deep jets on gas-giant planets. *Icarus* 194, 597-615.
- Liu, J., Goldreich, P. M., Stevenson, D. J., Aug. 2008, Constraints on deep-seated zonal winds inside Jupiter and Saturn. *Icarus* 196, 653-664.
- Lorenzen, W., Holst, B., Redmer, R., Dec. 2011, Metallization in hydrogen-helium mixtures. *Physical Review B: Solid State* 84 (23), 235109.
- Nettelmann, N., Becker, A., Holst, B., Redmer, R., May 2012, Jupiter Models with Improved Ab Initio Hydrogen Equation of State (H-REOS.2). *Astrophysical Journal* 750, 52.
- Olson, P., Christensen, U., Glatzmaier, G. A., May 1999, Numerical modeling of the geodynamo: Mechanisms of field generation and equilibration. *Journal of Geophysical Research* 104, 10383-10404.
- Rüdiger, G., Elstner, D., Ossendrijver, M., Jul. 2003, Do spherical α^2 -dynamos oscillate? *Astronomy and Astrophysics* 406, 15-21.
- Sanchez Lavega, A., Jan. 1982, Motions in Saturn's atmosphere - Observations before Voyager encounters. *Icarus* 49, 1-16.
- Schrinner, M., Petitdemange, L., Dormy, E. J., Jun. 2012, Dipole Collapse and Dynamo Waves in Global Direct Numerical Simulations. *Astrophysical Journal* 752, 121.
- Simitev, R. D., Busse, F. H., Jan. 2009, Bistability and hysteresis of dipolar dynamos generated by turbulent convection in rotating spherical shells. *EPL (Europhysics Letters)* 85, 19001.
- Stanley, S., Glatzmaier, G. A., May 2010, Dynamo Models for Planets Other Than Earth. *Space Science Reviews* 152, 617-649.
- Vasavada, A. R., Showman, A. P., Aug. 2005, Jovian atmospheric dynamics: an update after Galileo and Cassini. *Reports on Progress in Physics* 68, 1935-1996.
- Wicht, J., Oct. 2002, Inner-core conductivity in numerical dynamo simulations. *Physics of the Earth and Planetary Interiors* 132, 281-302.
- Williams, G. P., Aug. 1978, Planetary circulations. I - Barotropic representation of Jovian and terrestrial turbulence. *Journal of Atmospheric Sciences* 35, 1399-1426.

Table 2: Summary of the time-averaged results

*no-slip top boundary

** $a=25$ ***case from [Heimpel and Gómez Pérez \(2011\)](#) with $\eta=0.35$

Model	$\chi_m(\%)$	N_ρ	$\frac{Ra}{Ra_{cr}}$	E	Pm_i	N_r	l_{max}	Dipolarity	SD_{dip}	Ro_{zon}	Rm	Ro_ℓ	Λ	τ
01	80	0.0	11.5	10^{-4}	2.0	73	106	4.26×10^{-2}	4.73×10^{-2}	8.73×10^{-3}	115	1.84×10^{-2}	0.225	3.6
02	80	0.0	17.2	10^{-4}	2.0	73	106	8.13×10^{-2}	9.46×10^{-2}	1.41×10^{-2}	176	3.02×10^{-2}	0.727	1.4
03	80	0.0	23.0	10^{-4}	2.0	73	106	7.78×10^{-2}	9.24×10^{-2}	1.80×10^{-2}	221	4.13×10^{-2}	1.238	3.4
04*	80	0.0	23.0	10^{-4}	2.0	73	106	6.94×10^{-2}	8.43×10^{-2}	5.45×10^{-3}	180	6.34×10^{-2}	0.190	1.5
05	80	0.0	45.9	10^{-4}	2.0	81	170	1.53×10^{-1}	1.49×10^{-1}	3.09×10^{-2}	365	7.55×10^{-2}	2.906	1.0
06	90	0.0	11.5	10^{-4}	2.0	73	106	4.89×10^{-2}	6.07×10^{-2}	6.86×10^{-3}	143	2.39×10^{-2}	0.429	2.9
07*	90	0.0	11.5	10^{-4}	2.0	73	106	8.63×10^{-1}	2.92×10^{-2}	1.52×10^{-3}	113	2.65×10^{-2}	1.576	2.9
08*	90	0.0	23.0	10^{-4}	2.0	73	106	1.65×10^{-1}	1.50×10^{-1}	4.63×10^{-3}	237	6.45×10^{-2}	0.579	2.2
09d	95	0.0	11.5	10^{-4}	2.0	73	85	8.24×10^{-1}	5.75×10^{-2}	1.61×10^{-3}	127	2.72×10^{-2}	1.836	3.3
09m	95	0.0	11.5	10^{-4}	2.0	73	106	1.64×10^{-1}	9.20×10^{-2}	6.42×10^{-3}	158	2.66×10^{-2}	0.509	2.1
10	95	0.0	17.2	10^{-4}	2.0	73	106	8.10×10^{-2}	7.82×10^{-2}	8.23×10^{-3}	227	4.46×10^{-2}	1.295	1.8
11	95	0.0	23.0	10^{-4}	2.0	73	106	7.24×10^{-2}	7.83×10^{-2}	9.44×10^{-3}	282	5.83×10^{-2}	2.156	1.4
12	80	1.0	5.2	10^{-4}	2.0	73	106	1.59×10^{-2}	3.12×10^{-2}	8.30×10^{-3}	97	2.24×10^{-2}	0.230	4.3
13	80	1.0	10.3	10^{-4}	2.0	73	106	1.40×10^{-1}	1.40×10^{-1}	2.12×10^{-2}	220	5.31×10^{-2}	1.256	2.0
14d	90	1.0	5.2	10^{-4}	2.0	73	85	8.74×10^{-1}	2.83×10^{-2}	1.89×10^{-3}	104	3.35×10^{-2}	1.918	1.8
14m	90	1.0	5.2	10^{-4}	2.0	73	85	8.12×10^{-2}	1.08×10^{-1}	4.72×10^{-3}	125	3.47×10^{-2}	0.602	1.4
15*	90	1.0	5.2	10^{-4}	2.0	73	85	8.36×10^{-1}	3.68×10^{-2}	1.69×10^{-3}	113	3.68×10^{-2}	2.144	2.0
16	90	1.0	7.8	10^{-4}	2.0	73	106	4.70×10^{-2}	5.80×10^{-2}	8.94×10^{-3}	208	5.43×10^{-2}	1.526	1.8
17d	95	1.0	4.1	10^{-4}	2.0	73	85	8.29×10^{-2}	4.76×10^{-2}	1.29×10^{-3}	91	2.64×10^{-2}	1.251	1.2
17m	95	1.0	4.1	10^{-4}	2.0	73	85	1.21×10^{-1}	9.57×10^{-2}	3.08×10^{-3}	106	2.52×10^{-2}	0.408	1.2
18d	95	1.0	5.2	10^{-4}	2.0	73	106	8.33×10^{-1}	4.08×10^{-2}	1.59×10^{-3}	123	3.81×10^{-2}	2.346	2.6
18m	95	1.0	5.2	10^{-4}	2.0	73	106	3.40×10^{-2}	4.54×10^{-2}	3.67×10^{-3}	145	4.16×10^{-2}	0.770	2.4
19	95	1.0	7.8	10^{-4}	2.0	73	85	3.86×10^{-2}	4.81×10^{-2}	1.00×10^{-2}	253	6.33×10^{-2}	1.892	1.1
20	95	2.0	2.9	10^{-4}	2.0	73	106	1.94×10^{-2}	2.08×10^{-2}	4.64×10^{-3}	121	3.91×10^{-2}	0.522	2.4
21	70	3.0	4.3	10^{-4}	2.0	73	106	1.60×10^{-1}	1.77×10^{-1}	2.57×10^{-2}	95	2.26×10^{-2}	0.204	1.6
22	80	3.0	3.2	10^{-4}	2.0	73	85	1.33×10^{-1}	9.52×10^{-2}	1.39×10^{-2}	78	2.45×10^{-2}	0.210	3.7
23	80	3.0	4.3	10^{-4}	2.0	73	106	2.90×10^{-1}	2.13×10^{-1}	1.98×10^{-2}	125	4.25×10^{-2}	0.538	3.9
24**	80	3.0	4.3	10^{-4}	2.0	121	106	2.31×10^{-1}	2.07×10^{-1}	2.20×10^{-2}	115	3.76×10^{-2}	0.448	2.6
25*	80	3.0	4.3	10^{-4}	2.0	73	106	1.67×10^{-1}	1.42×10^{-1}	8.51×10^{-3}	132	5.56×10^{-2}	0.747	1.6
26	80	3.0	8.6	10^{-4}	2.0	81	170	2.15×10^{-1}	1.84×10^{-1}	4.04×10^{-2}	276	8.57×10^{-2}	2.372	1.2
27	90	3.0	3.2	10^{-4}	2.0	73	85	5.22×10^{-2}	7.13×10^{-2}	9.37×10^{-3}	133	4.16×10^{-2}	0.633	2.4
28	95	3.0	3.2	10^{-4}	2.0	73	106	3.31×10^{-2}	6.71×10^{-2}	7.57×10^{-3}	165	6.00×10^{-2}	0.956	3.8
29	70	4.0	8.8	10^{-4}	2.0	81	170	1.64×10^{-1}	1.37×10^{-1}	4.63×10^{-2}	137	3.01×10^{-2}	0.422	1.7
30	80	4.0	4.4	10^{-4}	2.0	81	170	1.21×10^{-1}	1.22×10^{-1}	1.52×10^{-2}	67	1.71×10^{-2}	0.092	3.0
31	80	4.0	5.5	10^{-4}	2.0	81	170	5.04×10^{-1}	3.05×10^{-1}	2.01×10^{-2}	98	3.27×10^{-2}	0.381	2.3
32	80	4.0	8.8	10^{-4}	2.0	81	170	2.36×10^{-1}	1.85×10^{-1}	3.04×10^{-2}	176	5.45×10^{-2}	1.142	1.2
33	95	4.0	5.5	10^{-4}	2.0	81	170	6.73×10^{-4}	8.86×10^{-4}	9.73×10^{-3}	198	8.57×10^{-2}	1.626	1.3
34	80	5.0	7.4	10^{-4}	2.0	81	170	8.97×10^{-1}	2.12×10^{-2}	1.44×10^{-2}	71	3.33×10^{-2}	0.829	2.9
35**	80	5.0	7.4	10^{-4}	2.0	97	170	5.29×10^{-1}	2.44×10^{-1}	2.15×10^{-2}	69	2.11×10^{-2}	0.240	1.6
36d	80	5.0	9.3	10^{-4}	2.0	81	170	8.73×10^{-1}	1.64×10^{-2}	1.58×10^{-2}	94	4.60×10^{-2}	1.082	1.3
36m	80	5.0	9.3	10^{-4}	2.0	97	170	2.93×10^{-1}	2.28×10^{-1}	2.29×10^{-2}	104	4.34×10^{-2}	0.616	1.6
37	90	5.0	7.4	10^{-4}	2.0	97	170	3.15×10^{-2}	2.02×10^{-2}	1.02×10^{-2}	145	5.39×10^{-2}	1.135	1.1
38	90	5.0	9.3	10^{-4}	2.0	97	170	3.47×10^{-2}	3.29×10^{-2}	9.75×10^{-3}	180	7.43×10^{-2}	1.689	0.7
39	80	5.5	9.7	10^{-4}	2.0	97	170	9.14×10^{-1}	1.53×10^{-2}	1.39×10^{-2}	76	3.44×10^{-2}	0.820	1.4
40	80	0.0	7.2	10^{-5}	1.0	81	170	8.56×10^{-1}	2.40×10^{-2}	5.01×10^{-4}	79	7.44×10^{-3}	0.319	1.0
41	80	0.0	12.1	10^{-5}	1.0	81	170	8.45×10^{-1}	2.12×10^{-2}	1.01×10^{-3}	122	1.37×10^{-2}	1.090	0.9
42	95	0.0	5.8	10^{-5}	1.0	81	133	8.51×10^{-1}	1.16×10^{-2}	3.21×10^{-4}	97	7.05×10^{-3}	0.209	1.1
43	80	1.0	4.4	10^{-5}	1.0	81	170	9.25×10^{-1}	8.82×10^{-3}	1.55×10^{-3}	96	1.32×10^{-2}	0.538	1.1
44	80	1.0	6.7	10^{-5}	1.0	81	170	9.27×10^{-1}	1.21×10^{-2}	3.67×10^{-3}	162	1.99×10^{-2}	1.071	1.1
45	80	1.0	11.1	10^{-5}	1.0	97	170	6.13×10^{-2}	8.68×10^{-2}	7.19×10^{-3}	316	3.62×10^{-2}	0.763	0.2
46	80	2.0	3.6	10^{-5}	1.0	81	170	9.22×10^{-1}	7.91×10^{-3}	1.90×10^{-3}	74	1.31×10^{-2}	0.432	0.8
47	80	2.0	5.4	10^{-5}	1.0	81	170	8.84×10^{-1}	3.82×10^{-2}	4.79×10^{-3}	149	1.82×10^{-2}	0.485	1.5

Continued on next page

Model	$\chi_m(\%)$	N_ρ	$\frac{Ra}{Ra_{cr}}$	E	Pm_i	N_r	l_{max}	$Dipolarity$	SD_{dip}	Ro_{zon}	Rm	Ro_ℓ	Λ	τ
48	80	3.0	2.9	10^{-5}	1.0	81	170	9.50×10^{-1}	1.16×10^{-2}	4.58×10^{-3}	100	1.43×10^{-2}	0.348	1.5
49	80	3.0	3.9	10^{-5}	1.0	81	170	8.74×10^{-1}	3.05×10^{-2}	4.57×10^{-3}	144	2.42×10^{-2}	0.853	1.0
50***	80	0.0	7.2	10^{-5}	3.0	121	170	8.05×10^{-1}	1.46×10^{-2}	1.74×10^{-3}	306	1.20×10^{-2}	2.279	0.2